Journal of Geophysical Research: Oceans

RESEARCH ARTICLE
10.1029/2018JC014196

Oceanic Eddy Characteristics and Generation Mechanisms in the Kuroshio Extension Region

Jinlin Ji[1,2], Changming Dong[3,4,5], Biao Zhang[3,6], Yu Liu[3,5], Bin Zou[7], Gregory P. King[8], Guangjun Xu[3], and Dake Chen[2]

[1]College of Ocean and Earth Science, Xiamen University, Xiamen, China, [2]State Key Laboratory of Satellite Ocean Environment Dynamics, SIO/SOA, Hangzhou, China, [3]School of Marine Sciences, Nanjing University of Information Science and Technology, Nanjing, China, [4]Department of Atmospheric and Oceanic Sciences, University of California, Los Angeles, CA, USA, [5]Oceanic Modeling and Observation Laboratory, Nanjing University of Information Science and Technology, Nanjing, China, [6]Jiangsu Engineering Technology Research Center of Marine Environment Detection, Nanjing, China, [7]National Satellite Ocean Application Center, SOA, Beijing, China, [8]Institut de Ciències del Mar (ICM-CSIC), Barcelona, Spain

Key Points:
- We analyze eddy characteristics
- We examine the eddy impact on vertical stratification
- We discuss two eddy generation mechanisms and apply an eddy-resolved numerical product to quantitatively analyze eddy generation mechanisms

Correspondence to:
C. Dong and B. Zhang,
cmdong@nuist.edu.cn;
zhangbiao@nuist.edu.cn

Citation:
Ji, J., Dong, C., Zhang, B., Liu, Y., Zou, B., King, G. P., et al. (2018). Oceanic eddy characteristics and generation mechanisms in the Kuroshio Extension region. *Journal of Geophysical Research: Oceans*, *123*, 8548–8567. https://doi.org/10.1029/2018JC014196

Received 23 MAY 2018
Accepted 30 OCT 2018
Accepted article online 5 NOV 2018
Published online 26 NOV 2018

Abstract The Kuroshio Extension region is well known for its strong eddy activity. In this paper, using satellite altimetry-measured sea surface height anomaly data from 1993 to 2012 in an extended Kuroshio Extension region (140–180°E, 25–45°N), we analyze eddy characteristics: eddy size, polarity, lifetime, intensity, trajectory, and spatial and temporal distributions. Using temperature and salinity vertical profiles measured by Argo floats, we examine the eddy impact on vertical stratification. During the 20-year period, 7,574 eddies are identified (based on following complete eddy trajectories) with a lifetime equal to or longer than 4 weeks. The numbers of cyclonic and anticyclonic eddies are found to be approximately the same. The distribution of eddy sizes peaks at a radius of about 40 km. The radius at the peak is at the same order as the first baroclinic deformation radius or the horizontal shear scale of the Kuroshio flow. The normalized eddy statistical characteristics show that eddies have different characteristics at different stages of their lifetimes. Among eddies with lifetimes longer than 50 weeks, more anticyclonic (cyclonic) eddies are found north (south) of 35°N. In contrast, among eddies with lifetimes shorter than 20 weeks, more cyclonic (anticyclonic) eddies are found north (south) of 35°N. The asymmetric distribution of eddies suggests two different eddy generation mechanisms: (1) the development of meanders in the Kuroshio path leading to the pinch off of eddies with longer lifetime (larger size) and (2) horizontal shear instability (barotropic instability) leading to eddies of shorter life (smaller size). We further apply an eddy-resolved numerical product to quantitatively investigate the eddy generation mechanisms.

Plain Language Summary We analyze eddy characteristics with 20-year satellite data and examine the eddy impact on vertical stratification. Besides, through the statistic result, we propose two eddy generation mechanisms: flow horizontal shear-induced eddy generation and the meander of flow path leading to the eddy generation. And then, we further apply an eddy-resolved numerical product to quantitatively investigate the eddy generation mechanisms.

1. Introduction

As a ubiquitous phenomenon in the ocean, eddies play an important role in the transport and distribution of heat, salt, energy (Bishop et al., 2013; Chelton et al., 2007, 2011; Chen et al., 2011; Chen, Gan, et al., 2012; Chen, Wang, et al., 2012; Chu et al., 2014; Dong et al., 2014; Liu et al., 2017; Roemmich & Gilson, 2001; Stammer, 1997; Stammer et al., 2001; Volkov et al., 2008; Wang et al., 2012; Xu et al., 2016; Yang et al., 2015; Z. G. Zhang et al., 2014; Z. W. Zhang et al., 2014), and marine biological and chemical processes (e.g., Gaube et al., 2015; Gruber et al., 2011; Johnson & McTaggart, 2010; Kouketsu et al., 2016; Vaillancourt et al., 2003). Dong et al. (2014) suggest that the global oceanic eddy movement can significantly influence distribution of the heat and fresh water in the ocean. The Kuroshio Extension (KE) region, from Japan eastward to the mid-Pacific, is one of the two largest eddy kinetic energy (EKE) bands in the northern Pacific Ocean (the other being the subtropical frontal zone; Chow et al., 2017; Liu et al., 2012; Qiu & Chen, 2011; Yang et al., 2017). Eddy activities in the KE play an important role in the decade variations in the KE system circulation (Qiu & Chen, 2010, 2011) and air-sea interaction (Ma et al., 2015). Ma et al. (2015) found that the wind speed is enhanced (weakened) and the precipitation is increased (decreased) with the

presence of warm (cold) eddies. After the Kuroshio Current leaves the Japanese coast, it enters the open ocean where the constraint of topography is lost. Without this topographical constraint, the Kuroshio's path meanders. A large number of individual eddies have previously been detected using altimetry-measured sea surface height anomalies (SSHAs; Chu et al., 2017; Ichikawa & Imawaki, 1994; Itoh & Yasuda, 2010), satellite sea surface temperature data (Dong, Nencioli, et al., 2011), and drifter trajectories from the Global Drifter Program (GDP; Dong, Liu¸ et al., 2011). Prants et al. (2014) used the geostrophic current anomalies derived from the SSHA to calculate Lagrangian trajectories of synthetic particles in the KE region and to simulate the Fukushima-derived radionuclides, in which eddies can be well presented by Lyapunov map.

Itoh and Yasuda (2010) analyzed the characteristics of eddies using SSHA from 1992 to 2008 in the KE region by applying the Okubo-Weiss method. They found that, in the KE region, about half of the EKE variance is attributable to mesoscale eddies. Dong, Nencioli, et al. (2011) detected and analyzed eddies using AVHRR 9-km sea surface temperature data for the years between 2006 and 2009 and found more anticyclonic (cyclonic) eddies to the north (south) of the Kuroshio path. Dong, Liu, et al. (2011) analyzed an eddy data set for the KE region they derived from the Global Drifter Program (GDP) sea surface drifter trajectories.

However, these studies on the KE eddies, that is, Itoh and Yasuda (2010), Dong, Nencioli, et al. (2011), and Dong, Liu, et al. (2011), focused on either eddy statistical analysis or eddy detection method. The eddy generation mechanisms in the KE region, that is, around an oceanic jet in an open ocean, are not sufficiently stressed or emphasized. Moreover, how eddies affect the vertical profiles of the temperature and salinity in the KE is not explicitly clarified. Motivated by these questions, the present study analyzes the eddy data set from the SSHA data and further infers the eddy generation mechanisms in the KE region based on the eddy statistical analysis.

In this study, we first derive an eddy data set based on an automated eddy detection scheme (Nencioli et al., 2010) using altimetry SSHA data in the KE region for the 20-year period of January 1993 to December 2012. We then make a thorough statistical analysis of that data set. Subsequently, the impacts of eddies on the *T*/*S* vertical profiles are examined using collocated Argo temperature (*T*) and salinity (*S*) vertical profiles and the detected eddies. The results suggest two dominant eddy generation mechanisms, one of which produces shorter-lived eddies than the other.

The remainder of this paper is organized as follows: section 2 describes the data and methodology used in the paper. In section 3, the data set of eddies detected using the SSHA data is analyzed, and the impacts of eddies on the *T*/*S* vertical profiles are examined. Section 4 is Discussion, in which two eddy generation mechanisms are presented. Section 5 is the summary.

2. Data and Methodology

The following data are used in this study: altimetry SSHA and Argo floats. An automatic eddy detection scheme based on eddy geometry is employed.

2.1. Altimetry SSHA

The altimeter products are produced and distributed by Archiving, Validation and Interpretation of Satellite Oceanographic (AVISO; http://www.aviso.altimetry.fr/), as part of the Ssalto ground processing segment. SSHA data have a spatial resolution of 1/3° × 1/3° and a 7-day temporal sampling over the period from October 1992 to August 2013. We focus on the period of January 1993 to December 2012 over the KE region (25–45°N, 140–180°E).

2.2. Argo *T*/*S* Profiles

Argo floats collect vertical profiles of temperature (*T*) and salinity (*S*) from the upper 2,000 m of the ice-free global ocean. The *T*/*S* vertical profiles data can be downloaded from ftp://www.usgodae.org/pub/outgoing/argo/geo/pacific_ocean/. They are sampled daily and the maximum depth reachable by Argo floats is about 2,000 m. Spatial (center location and eddy boundary) and temporal information from the detected eddies are used as indices to identify the Argo vertical profiles collocated inside these eddies. There are 4,233/3,715 profiles trapped by anticyclonic/cyclonic eddies in the area of study. Beside this, there are 1,327/1,281 profiles inside anticyclonic/cyclonic eddies in the area [30–40°N], [145–165°E]. These profiles are used to examine the impact of eddies on the thermocline and halocline.

2.3. Numerical Model Data OFES

The numerical model data we use are the OFES (Ocean General Circulation Model for the Earth Simulation) data (Masumoto et al., 2004), which have horizontal spatial resolution of 0.1° and 54 vertical layers (with 5-m resolution at the surface, and the maximum depth is 6,065 m), resolving mesoscale eddies; the data can be downloaded from http://apdrc.soest.hawaii.edu/las_ofes/v6/dataset?catitem=87. We choose the data in year 2000 (3-day averaged) to estimate the EKE sources through the EKE evolution equation in KE region (25–45°N, 140–180°E) for the study.

2.4. A Velocity Geometry-Based Automated Eddy Detection Scheme

In this study, we use an eddy-detection algorithm based on eddy vector geometry proposed by Nencioli et al. (2010). This algorithm has been successfully applied to study eddies in different regions, for example, the lee side of Lanai Island, Hawaii (Dong et al., 2009), Southern California Bight (Dong et al., 2012), subtropical North Pacific Ocean (Liu et al., 2012), leeward of the Madeira Islands (Couvelard et al., 2012), Balearic Sea (Amores et al., 2013), Alboran Sea (Peliz et al., 2013), the global ocean (Dong et al., 2014), and South China Sea (Lin et al., 2015). The eddy detection scheme is briefly introduced below. For more details, readers can refer to Nencioli et al. (2010). First, four constraints on the geometry of velocity vectors are defined to determine an eddy center:

1. Along an east-west section, the v' component of velocity must reverse in sign across the eddy center, and its magnitude must increase away from the center.
2. Along a north-south section, the u' component of velocity must reverse in sign across the eddy center and its magnitude must increase away from the center. In addition, the sense of rotation for both u' and v' should be the same.
3. The eddy center is defined as the minimum velocity around a region, which extends up to a certain grid point.
4. The directions of two neighboring velocity vectors around the eddy center must change with a constant sense of rotation and lay within the same or two adjacent quadrants.

where u' and v' are the geostrophic current anomaly calculated from the AVISO SSHA data.

$$u' = -\frac{g}{f}\left(\frac{\partial h'}{\partial y}\right), \tag{1}$$

$$v' = \frac{g}{f}\left(\frac{\partial h'}{\partial x}\right), \tag{2}$$

where h' is the SSHA and f is the Coriolis parameter. Eddy centers are first defined at the points satisfied by all of the constraints listed above. We then search for the outermost closed streamline around the center. If velocity magnitudes cease to increase in the radial direction, it can be regarded as the eddy boundary. A tracking algorithm is also included in the package. We applied this method to 20 years (1993–2012) of altimetry SSHA-derived geostrophic velocity anomalies to obtain an eddy data set, which contains the location of the eddy center, its lifetime, type, size, intensity, and the locations of its boundaries.

2.5. EKE

The EKE at each point in space and time is calculated using the following formula:

$$EKE = \frac{1}{2}\left(u'^2 + v'^2\right), \tag{3}$$

where u' and v' are the geostrophic current anomaly calculated from the AVISO SSHA data. A spatial map of the EKE, averaged over all weeks in the study period after applying a 90-day high-pass filter to remove the influence of seasonal variability.

3. Results

3.1. EKE

Before we discuss the eddy detection results, we first examine the EKE, as it is often used to characterize the intensity of eddy activity. As shown in Figure 1, the EKE is much higher in the KE region than in the adjacent

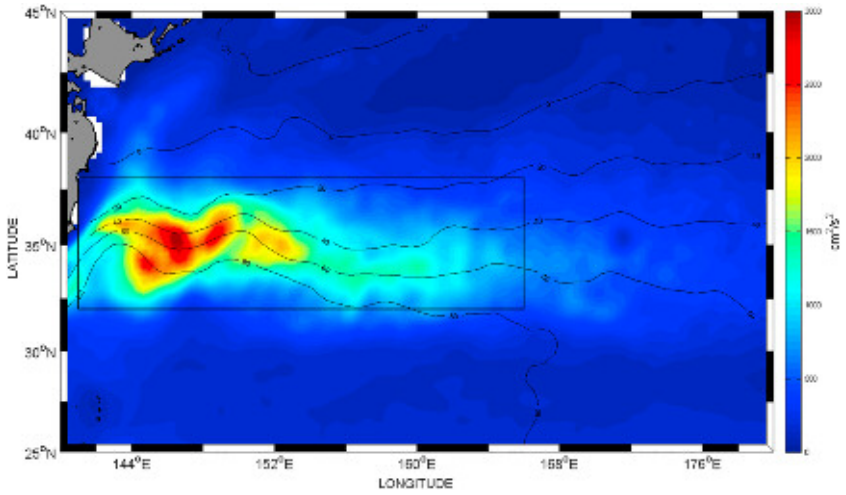

Figure 1. Spatial distribution of averaged eddy kinetic energy with 90-day high-pass filter over the period of January 1993 to December 2012 (cm^2/s^2). The geostrophic velocity anomalies are derived from Archiving, Validation and Interpretation of Satellite Oceanographic sea surface height anomaly data through geostrophic currents formulae, the black contours are the mean absolute dynamic height (Mean Absolute Dynamic Topography data from Archiving, Validation and Interpretation of Satellite Oceanographic website), and the black rectangle denotes the Kuroshio Extension region.

regions, which agrees with results as shown Qiu et al. (2015), who used Aviso SSH anomalies data for the period of October 1992 to December 2013.

Figure 2 shows the weekly time series of the total surface averaged EKE (red) and eddy-contributed surface-averaged EKE (blue) from January 1993 to December 2012. The seasonal and interannual variations of the EKE are also plotted in the upper and lower panels, respectively. The EKE caused by eddies is different from the total EKE. We define the former one as the EKE of an individual eddy: the average kinetic energy within an eddy area (from its boundary to its center). We found that eddy contribute about 70.1% of the total EKE (Figure 2). Both the total EKE and eddy-contributed EKE have the same seasonal variation and high interannual correlation of 0.77. The upper panel shows that the seasonal variation is smallest in February (winter) and largest in August (summer), which agrees with results from Scharffenberg and Stammer (2010), who used altimeter data from four satellites for the period of 2002–2005. The lower panel shows the interannual variation of EKE: The dashed line denotes the weekly sampled variation, and the solid line represents the yearly

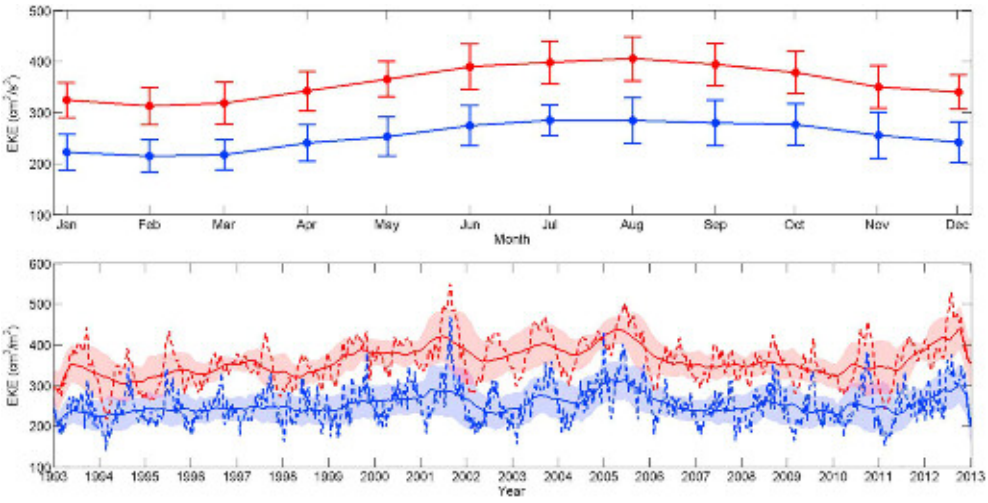

Figure 2. Time series of total surface averaged EKE (red) and eddy-contributed surface-averaged EKE (blue): monthly (top) and temporal (bottom) in [25–45°N], [140–180°E]. The upper panel shows the monthly climatological EKE. The solid lines (dashed lines) in the lower panel represent 52-week moving average (temporal) situation (cm^2/s^2). Shaded is the standard deviation. EKE = eddy kinetic energy.

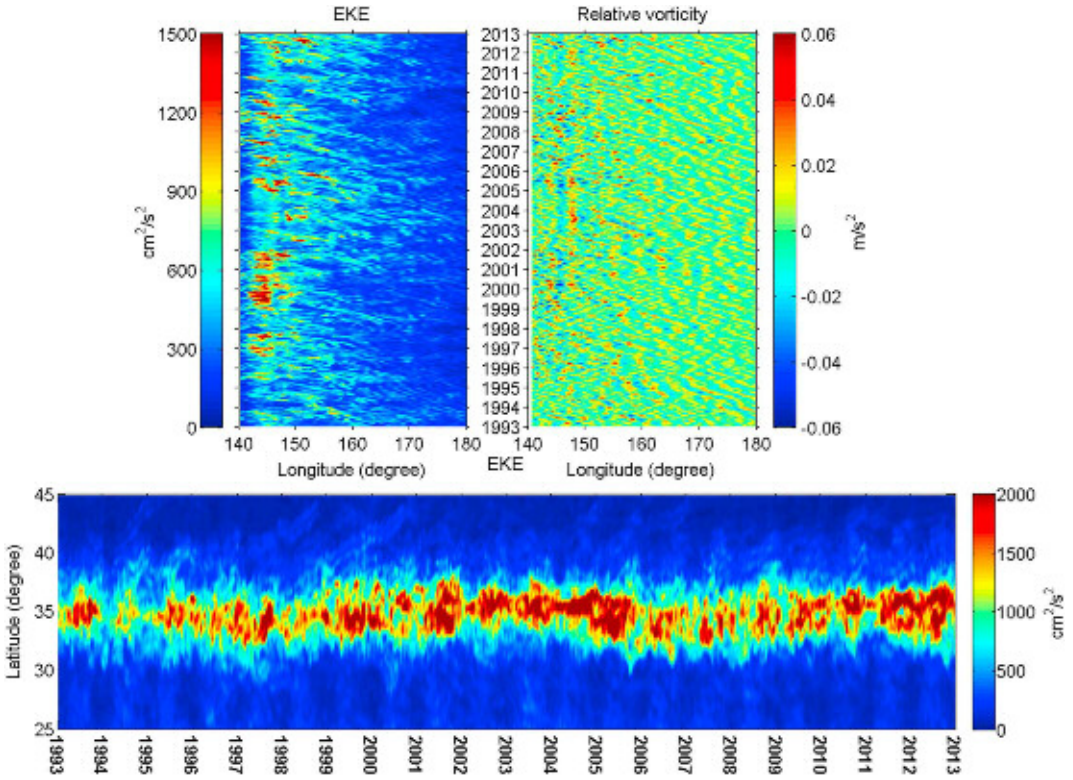

Figure 3. The spatial distribution of EKE and relative vorticity as functions of time (Hovmöller plots). In the upper panels, EKE (left) and relative vorticity normalized by the background Coriolis parameter (right) are averaged over latitudes 25–45°N and plotted as a function of longitude and time. The bottom panel shows a function of latitude and time. EKE = eddy kinetic energy.

variation from a 52-week moving average filter. It is shown that the yearly EKE is highest between 2000 and 2005. According to Chen et al. (2018), both local and remote wind forcing and ocean internal instability is responsible for the generation and modulation of EKE. We calculate the correlation coefficient between the Nino 3.4 index and monthly averaged EKE, but a low correlation (0.026) between them is found, it indicates that there is no significant correlation between the EKE and ENSO events in our study region.

Figure 3 shows the spatial and temporal variation of EKE and (normalized) relative vorticity in the KE region. The upper two panels show Hovmöller plots (meridional-averaged quantities as a function of longitude and time), which illustrate the zonal propagation of EKE and relative vorticity in the KE region. The westward propagation speeds of both vorticity and EKE are about 4.7 cm/s. It should be noted that the EKE contains contributions from processes that deviate from the mean state, including frontal bending, fluctuation, unstable wave, and meander of the Kuroshio front (Waterman et al., 2011). Therefore, one should take care when interpreting the EKE variability shown in Figure 3, as it is somewhat inconsistent with that obtained from EKE calculations with the population of individual eddies. The bottom panel in Figure 3 shows the time series of zonally averaged EKE against latitude, which clearly shows that the largest EKE appears along latitude 35°N.

3.2. Eddy Size, Lifetime, and Vorticity

Two eddy counting methods are developed: Eulerian method and Lagrangian method. To find out how many eddies exist in each moment, the former method is used. However, if information about an eddy generation, evolution, and termination is required, the latter method is employed to identify the eddy history. The Lagrangian method can also be used to remove those eddies whose lifetimes are shorter than 4 weeks. We detected a total of 14,797 eddy tracks with the trajectory method. Slightly more than half were identified as cyclonic eddy tracks (7,669; 51.8%) and the remainder as anticyclonic eddy tracks (7,128; 48.2%). By means of the snapshot method, the total number of eddies identified was 122,479. About half of these (61,679; 50.4%) were identified as cyclonic eddies, and the remainder as anticyclonic eddies (60,800; 49.6%). Due to

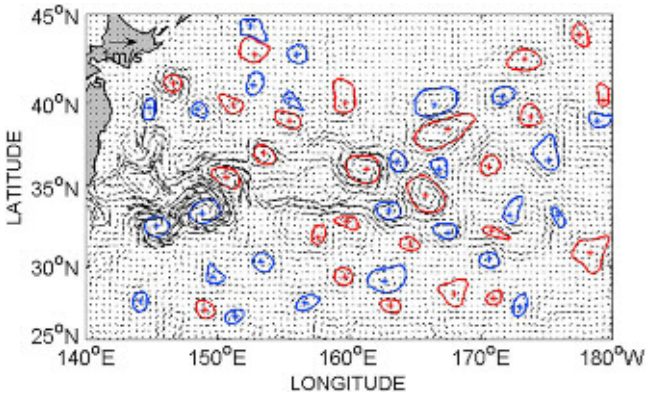

Figure 4. A snapshot (6 May 2009) of the geostrophic velocity anomaly field derived from Archiving, Validation and Interpretation of Satellite Oceanographic sea surface height anomaly data and eddies with radius larger than 50 km, identified by their center and boundary curves: Cyclonic (anticyclonic) eddies centers and boundary curves are shown in blue (red).

possible errors in identification and limitations of altimeter SSHA data, we only consider (except where otherwise specified) those eddies surviving longer than or equal to 4 weeks. Based on this 4-week criterion, the number of eddies identified by the trajectory method drops to 7,574, and the number identified by the snapshot method drops to 109,952. For both methods, the split between cyclonic and anticyclonic remains close to 50/50. As an example to demonstrate how eddies are identified, Figure 4 shows a snapshot of 6 May 2009 for detected eddies with a radius larger than 50 km, overlaid with geostrophic current anomaly vector field derived from SSHA data.

Figure 5 shows the time series of eddy number identified with the snapshot method. The left panel shows the seasonal variation, and the right panel is the interannual variation. Figure 5 (left) shows that the number of eddies in March is the largest, and Figure 5 (right) shows there are more eddies between 1995 and 1999 than in other years.

In order to examine the spatial distribution of eddy sizes in the KE, we divide the study area into 1° × 1° bins. The radius of all eddies whose centers are located in each 1° × 1° bin are averaged to represent the eddy size in that bin. The results (not shown) are similar to Itoh and Yasuda (2010): The larger eddies are located along 35°N, with the larger cyclonic (anticyclonic) eddies located south (north) of 35°N. From Figure 3 (bottom panel), we see that latitude 35°N can be regarded as the climatological mean location of the main axis of the Kuroshio. Therefore, we conclude that the larger cyclonic eddies appear in the south, and the larger anticyclonic eddies appear north of 35°N, which is in agreement with the results of Itoh and Yasuda (2010).

Radius and lifetime are two important parameters characterizing an eddy. Figure 6 shows the histograms of eddy radius (upper panel) and eddy lifetimes (lower panel). The histograms of the eddy radius show that the anticyclonic and cyclonic distributions are similar, with both having peak at about 40 km. The radius at the peak is of the same order as either the horizontal shear scale of the Kuroshio or first baroclinic deformation radius (see Chelton et al., 1998), which implies that the shear instability or the baroclinic instability could be responsible for the eddy generation. For more discussion, please see section 4.

The eddy lifetime distributions are shown in the lower panel of Figure 6: anticyclonic eddies (gray) and cyclonic eddies (black). Eddies can live up to 160 weeks and anticyclonic eddies tend to live longer than cyclonic eddies. It has been demonstrated in previous numerical and theoretical studies, such as Graves et al. (2006), Perret et al. (2006), and Dong and Chan (2007), that anticyclonic eddies become more coherent while cyclonic eddies elongate and weaken. With a review of the computational literature, Graves et al. (2006) theoretically explains why anticyclonic vortices are less strongly deformed than cyclones during transient straining events and thus lose energy and potential enstrophy in relaxing back to the equilibrium axisymmetric state.

The intensity of an eddy can be characterized by its EKE and vorticity. The vorticity reaches a maximum at the eddy center and a minimum at its boundary. In this study, the vorticity of an eddy is approximated by the vorticity at the eddy center. A histogram of anticyclonic and cyclonic eddy relative vorticity, normalized by the local Coriolis parameter f is shown in Figure 7. There are slight differences between the two vorticity distributions: For large vorticity magnitudes, there are more cyclonic than anticyclonic eddies.

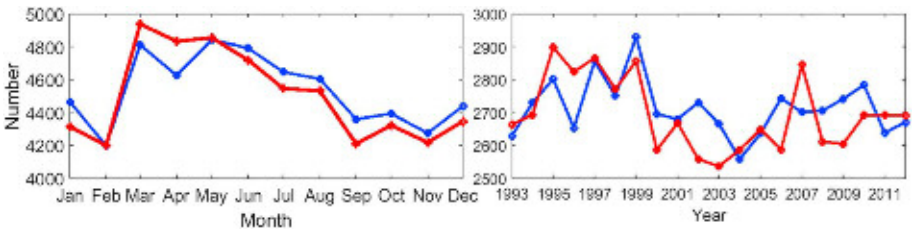

Figure 5. Seasonal (left) and interannual (right) variations in eddy number in the Kuroshio Extension region. Cyclonic eddy numbers are plotted with a blue line and anticyclonic eddy numbers with a red line.

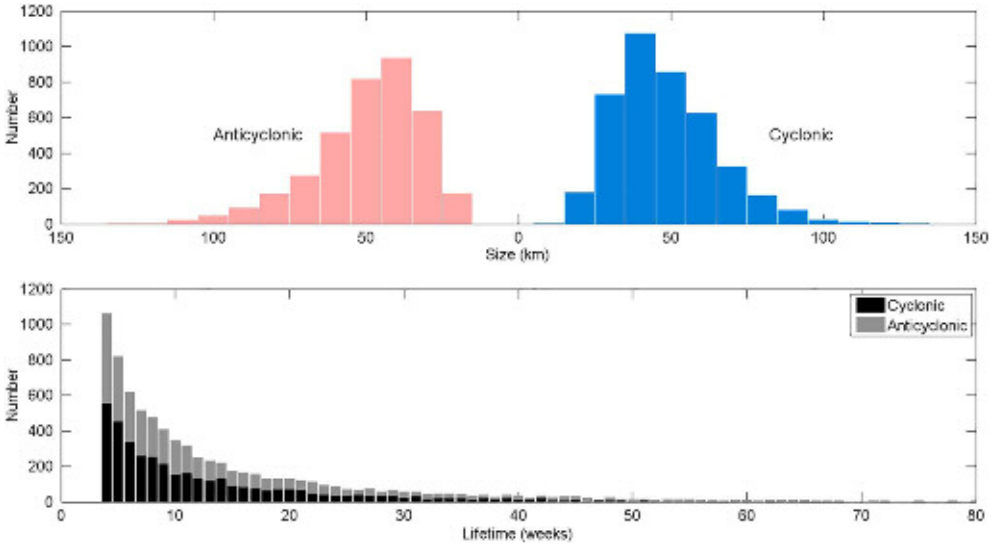

Figure 6. Histograms of eddy radius (top panel) and eddy lifetimes (bottom panel).

On the left panel of Figure 8, the zonally averaged normalized relative vorticity is plotted against latitude. The peak cyclonic eddy vorticity lies south of the Kuroshio axis, while the peak anticyclonic eddy vorticity lies to its north. On the right panel of Figure 8, the meridionally averaged normalized relative vorticity is plotted against longitude. It shows that the vorticity of both the cyclonic and anticyclonic eddies decreases eastward. The results shown in Figure 8, together with the results of the spatial distribution of eddy radius, demonstrate that the cyclonic (anticyclonic) eddies located in the south (north) area of the Kuroshio main axis are larger and stronger than the anticyclonic (cyclonic) eddies, which agrees with Itoh and Yasuda (2010).

3.3. Eddy Propagation

Figure 9 shows the propagation speeds of both cyclonic and anticyclonic eddies as a function of latitude. In general, the zonal (westward) speed decreases with latitude and has a range of about 1–6 cm/s, which is of the same order as the propagation speed of Rossby wave. In particular, it is noted that the zonal (westward) speed is almost 0 at 35°N. North of the Kuroshio climatological mean axis, there is a peak in the eddy zonal (westward) speed at 36°N. Anticyclonic eddies display similar propagation speed with cyclonic eddies. South of the Kuroshio climatological mean axis, the zonal (westward) speed reaches its maximum value at about 30°N. Except near the boundary latitudes, the cyclonic eddies persistently move southward, while the anticyclonic eddies move northward (southward) to the north (south) of about 33°N.

3.4. Eddy Evolution

In the above sections, eddies have been characterized using the definitions given in sections 3.1 and 3.2 for intensity (vorticity and EKE) and radius. Here we define and calculate EKE differently—EKE of an individual eddy: the average kinetic energy within an eddy area (from its boundary to its center). The vorticity of an eddy

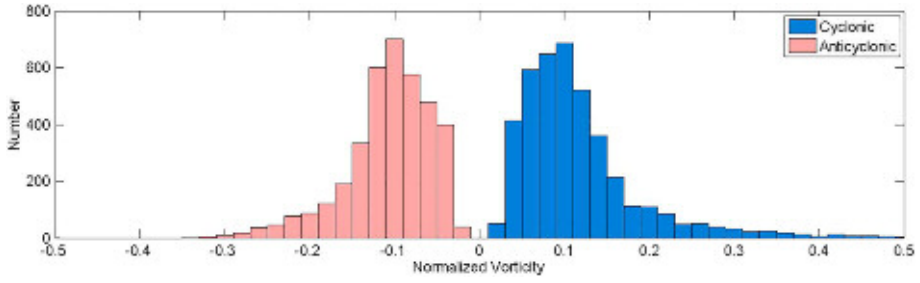

Figure 7. Histograms of normalized relative vorticity (relative vorticity divided by the local Coriolis parameter *f*): anticyclonic (pink) and cyclonic (blue).

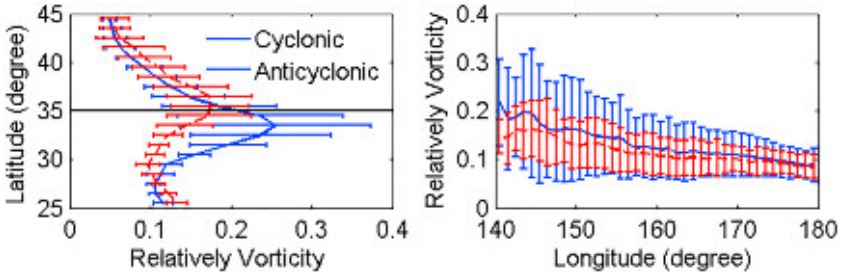

Figure 8. The left panel shows the variation of the zonally averaged vorticity with latitude, and the right panel the variation of the meridionally averaged vorticity with longitude. The blue and red lines denote cyclonic and anticyclonic eddies, respectively.

is defined as previously stated: the vorticity at the eddy center. We also consider the eddy deformation rate S, defined by $S = (S_n^2 + S_s^2)^{1/2}$, where shear deformation rate S_n

$$S_n = \frac{\partial u'}{\partial x} - \frac{\partial v'}{\partial y} \tag{4}$$

and the stretching deformation rate S_s

$$S_s = \frac{\partial v'}{\partial x} + \frac{\partial u'}{\partial y} \tag{5}$$

(Carton, 2001; Okubo, 1970; Weiss, 1991). The u' and v' are the geostrophic current anomalies. The evolutions of the normalized vorticity, EKE, radius, and deformation rate are recorded for each eddy throughout its lifetime. Only eddies with lifetimes longer than 20 weeks are considered to represent the general patterns of the time evolution of these four parameters over an eddy lifetime. In total there are 772 cyclonic eddies and 806 anticyclonic eddies. In order to compare eddies with different lifespans, the time along an eddy track is normalized by that eddy's lifespans: youth stage (0–1/5), mature stage (1/5–4/5), and old stage (4/5–1). Similarly, each of the four parameters is normalized by its maximum value within each eddy lifetime. The resulting temporal evolution of the four parameters is shown in Figure 10. The figure shows that the eddy vorticity magnitude, EKE, and eddy size increase during the youth stage, slightly increase throughout the mature stage,

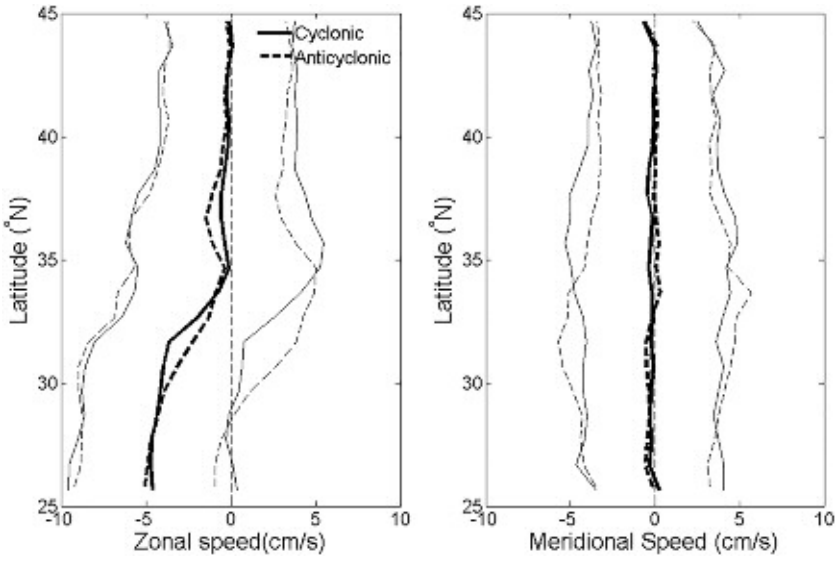

Figure 9. Variation with latitude of anticyclonic (black solid line) and cyclonic (black dashed line) eddy zonal and meridional propagation speeds. The gray solid and dashed lines are their standard deviation interval.

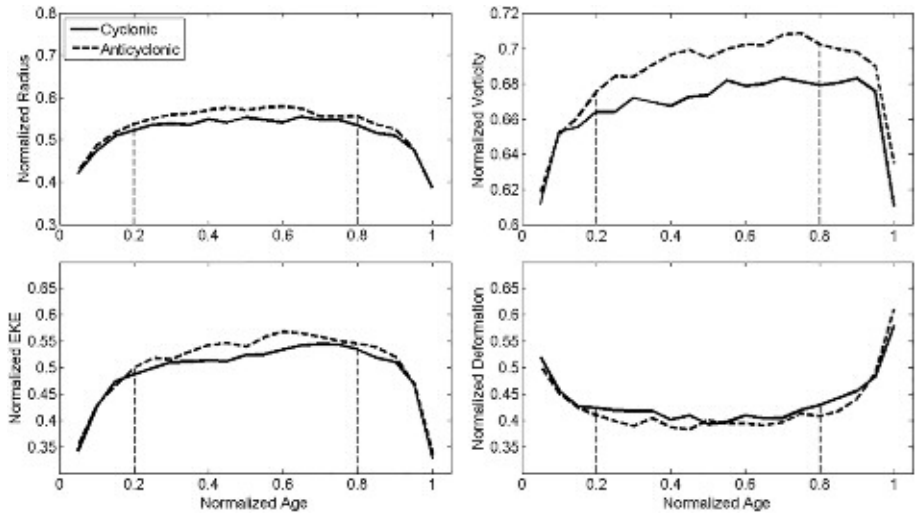

Figure 10. Time evolution of the mean eddy characteristic parameters: radius (upper left), vorticity (upper right), kinetic energy (lower left), and deformation (lower right). Only eddies with life spans longer than 20 weeks are included in the analysis. Each eddy's age is normalized by its life span. For each eddy, each parameter is normalized by its maximum value within the eddy lifetime. The solid and dashed lines indicate cyclonic and anticyclonic eddies, respectively.

and then decrease sharply in old age. It is interesting to notice that there is a slight increase in the intensity (EKE or vorticity) of eddies, which shows that eddies continue to extract energy from the mean stream (Kuroshio) during their mature stages before starting to decay. The opposite trend occurs for the deformation rate: In the first 1/5 of an eddy lifetime, the rate decreases (tends to move to a perfect circle), then stays approximately constant for the next 3/5 of the lifetime; and in the final 1/5 of an eddy lifetime (old age), the rate increases sharply until the eddy disappears (death). Liu et al. (2012) reported the same pattern of parameter evolution in their eddy analysis of the subtropical frontal zone.

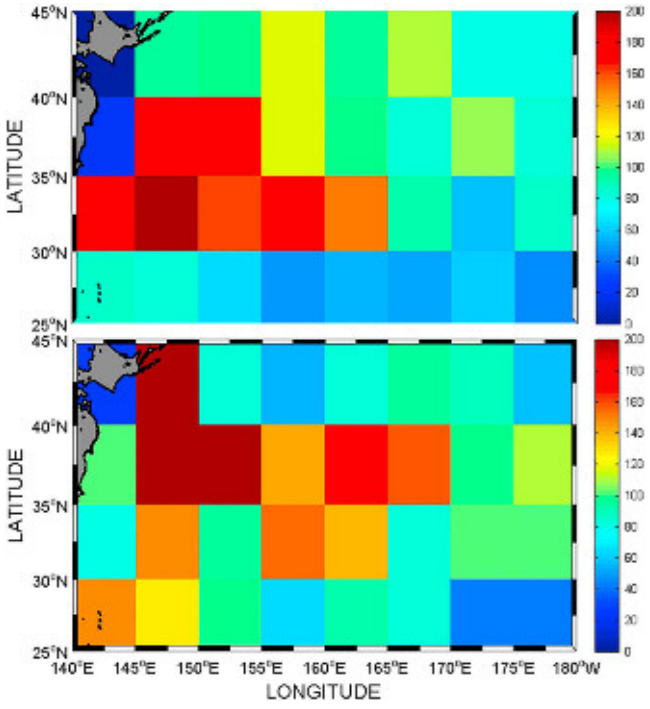

Figure 11. Spatial distribution of the number of Argo profiles trapped within cyclonic eddies (top) and anticyclonic eddies (bottom). The bin size is 5° × 5°.

3.5. Vertical Profiles of *T/S* Affected by Eddies

To this point we have examined the sea surface characteristics of eddies using altimetry data. In this section, we use Argo float data to investigate variations of eddy *T/S* vertical profiles caused by eddies. First, all Argo floats from 1999 to 2010 trapped by the detected eddies in the KE region are identified. Figure 11 shows the spatial distribution of the number of Argo floats trapped in detected eddies in 5° × 5° bins. In the KE region, there are 4,233 and 3,715 profiles of Argo floats trapped by anticyclonic and cyclonic eddies, respectively. This indicates there is a sufficient amount of data to obtain good statistics on the eddy impacts on *T/S* vertical profiles. From Figure 11, one can see that more Argo vertical floats are trapped by anticyclonic (cyclonic) eddies in the north (south) of the KE main axis. We find that 1,355 anticyclonic and 1,112 cyclonic eddies trap at least one Argo float, which indicates that some eddies have multiple floats and hence multiple *T/S* vertical profiles. The *T/S* anomaly (with respect to the mean in each bin) vertical profiles in the bins spanning only the region [30–40°N] and [145–165°E] are shown in Figure 12. These four panels show that an eddy can induce an anomalous *T/S* vertical profile, and cyclonic and anticyclonic eddies can cause negative and positive *T/S* anomalies, respectively. The lower left panel shows that temperature anomalies initially increase, reach a maximum, and then decrease, for both the cyclonic and anticyclonic eddies. The depth at which the profiles reach a maximum is about 350 m for cyclonic eddies and 380 m for anticyclonic eddies. Eddies have a similar effect on salinity anomaly profiles (300 m for cyclonic eddies and 320 m for anticyclonic eddies). Several researchers

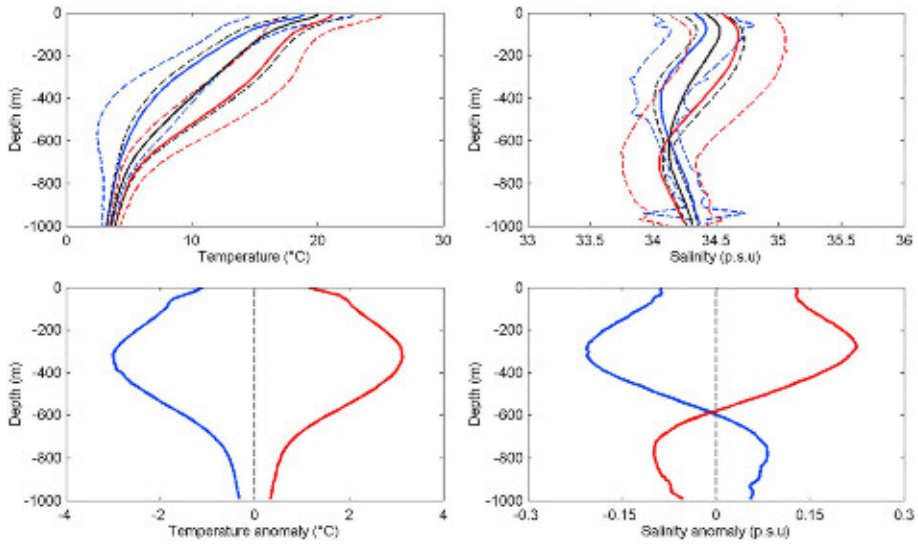

Figure 12. Vertical profiles of *T*/*S* affected by eddies. Bin-averaged *T*/*S* vertical profiles from Argo data in the bin located at [30–40°N], [145–165°E]: temperature (upper left), salinity (upper right), temperature anomaly (bottom left), and salinity anomaly (bottom right). The blue and red lines represent cyclonic and anticyclonic eddies, respectively, and the black solid lines are the means from all profiles. The dash lines indicate their standard deviation interval.

previously reported the *T*/*S* vertical profiles inside eddies. Result from Liu et al. (2012) show that the peak of *T*/*S* anomaly vertical profiles inside eddies can reach a depth of 180/200 m in the subtropical region. Further, Chen et al. (2011) investigated the eddy impact on the thermohaline in the South China Sea. They found that anticyclonic eddies can cause a larger positive temperature anomaly in the upper 500 m and the most significantly affected depth is 110 m, whereas cyclonic eddies obviously affect the temperature structure in the upper 160 m and the most affected depth is 80 m. Pegliasco et al. (2015) conducted studies about eddy vertical structures observed in four major Eastern Boundary Upwelling Systems. When comparing our results to past literature, we noticed that regardless of the *T*/*S* vertical profiles anomaly depth caused by eddies or the depth corresponding to the peak anomaly value, they are always larger than in other regions. This may be due to the stronger EKE and deeper thermocline in the western boundary regions than in other regions. Besides, in the western boundary regions, eddy intensity and structure are also stronger and more cohesive than in other regions. Note that the *T*/*S* anomaly vertical profiles for anticyclonic and cyclonic eddies are almost mirror reflections of one another.

4. Discussion

4.1. Eddy Generation Mechanisms

The KE region is in the open ocean far from the constraints of topography. Eddy generation mechanisms in this region are complex. In this section, we attempt to infer the eddy generation mechanisms from the eddy statistical characteristics.

Figure 13. Eddy generation mechanisms: (a) eddies generated through the jet path meandering, and (b) eddies generated through horizontal shear instability.

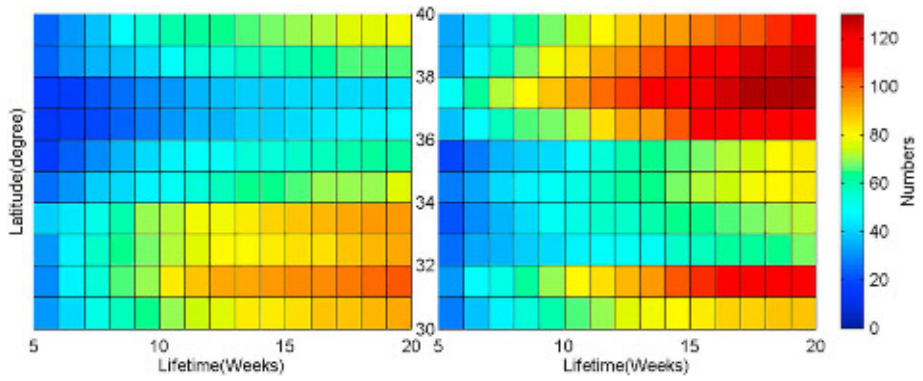

Figure 14. Latitudinal variation of the number of eddies with lifetimes shorter than 20 weeks: anticyclonic (left panel) and cyclonic (right panel).

The relationship between the KE meander and eddy formation in the KE region has been discussed in the literature. There are two aspects in the relationship. The one aspect is that the development of the jet meander could lead to the eddy formation, which can be approved using specific cases or numerical modeling. The other aspect is that the presence of one eddy on one side of the jet (Kuroshio) could cause the straight jet to lose the pressure balance and then trigger the meander of the Kuroshio path, such as Bishop, 2013; Hurlburt et al., 1996; Ichikawa & Imawaki, 1994; Itoh & Yasuda, 2010; Kobashi et al., 2016; Mishra et al., 1999; Mitsudera et al., 2001; Miyazawa et al., 2004, 2008, Mizuno & White, 1983; Qiu & Chen, 2005, 2010; Waseda et al., 2003; and Yasuda et al., 1992. In this study, we propose two eddy generation mechanisms: flow horizontal shear-induced eddy generation and the meander of flow path leading to the eddy generation; see Figure 13.

According to the flow instability theory (Drazin & Reid, 1981), considering all scales of perturbations, only the most unstable mode with the same scale as its shear scale can survive. Based on this fact, we make two assumptions to infer the first eddy generation mechanism from the eddy data set, that is, the shear instability:

1. The Kuroshio is a jet with current shears on both sides. We assume that the shear could cause the instability, which will lead to the eddy generation. The eddy size should be in the same as the shear scale. Moreover, if eddies are generated by the shear instability of the Kuroshio Current in the KE

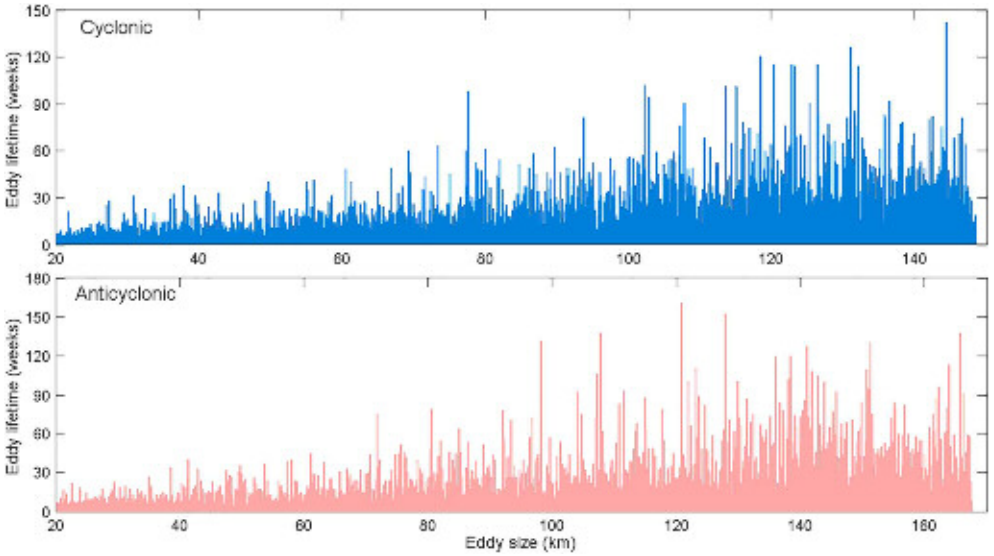

Figure 15. Relationship between eddy lifetime and eddy radius: cyclonic (upper) and anticyclonic (lower).

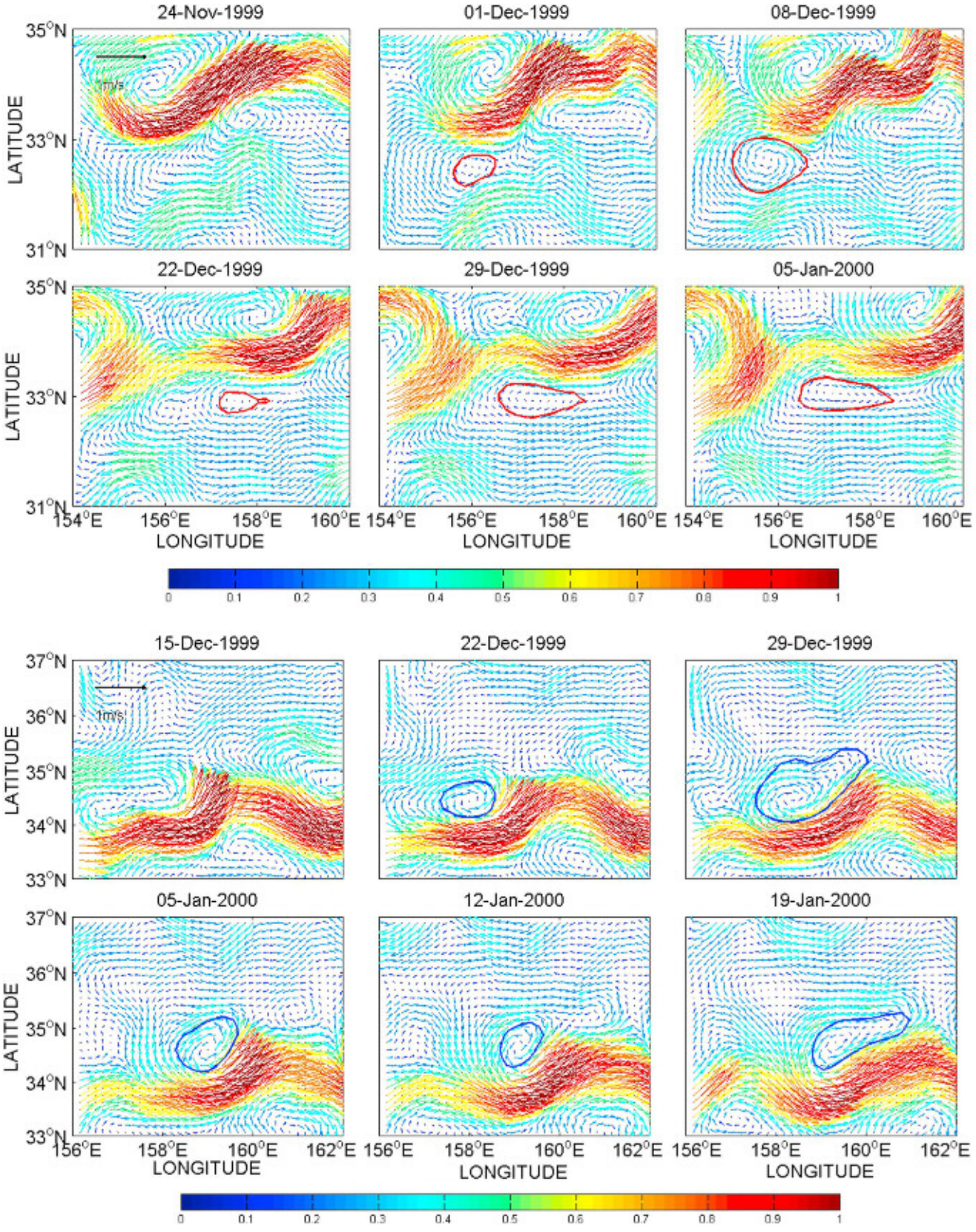

Figure 16. Shear instability-generated eddy. Vectors are Archiving, Validation and Interpretation of Satellite Oceanographic surface geostrophic velocity anomalies. The figure sequence in the upper panel shows an anticyclonic eddy (red ring), and the sequence in the lower panel shows a cyclonic eddy (blue ring).

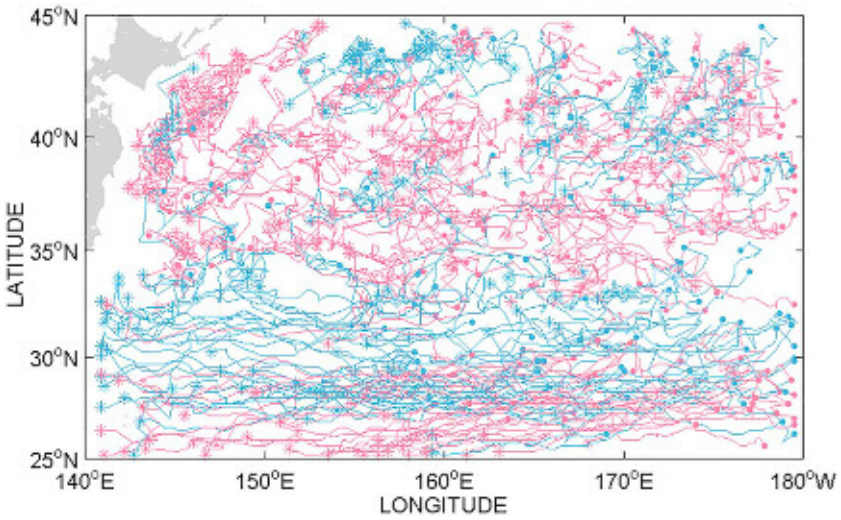

Figure 17. Eddy trajectories for eddies with lifetimes longer than 50 weeks. The dots and asterisks indicate the generation and termination points of each eddy trajectory, respectively. The red lines are anticyclonic eddies and blue lines are cyclonic eddies.

region, cyclonic (anticyclonic) eddies should be found on the northern (southern) side of the Kuroshio.

2. From the eddy statistical analysis, we found that most cyclonic (anticyclonic) eddies with lifetimes shorter than 20 weeks are located on the northern (southern) side of the Kuroshio (Figure 14). The relationship between the eddy size and eddy lifetime shown in Figure 15 demonstrates that the eddy radius ranges between 40 and 60 km when the eddy lifetime is shorter than 20 weeks. Since the Kuroshio width is about 100 km and half of the width is the horizontal shear scale (50 km), the radius is therefore the same scale of the Kuroshio shear scale.
3. From the above two steps, we infer that eddies with lifetimes shorter than 20 weeks and whose sizes are in the same scale of Kuroshio shear scale are caused by the Kuroshio flow shear.

To further demonstrate this, Figure 16 plots two eddies cases (cyclonic and anticyclonic) generated on the northern and southern sides of the Kuroshio axis.

The second eddy generation mechanism is the meanders of Kuroshio path. We also make two assumptions to infer the eddy generation mechanism from the eddy data set:

1. There are two meandering directions for a zonal jet: northward and southward. We assume that if the meander grows large enough, it will lead to an eddy pinch off, and one should find more cyclonic (anticyclonic) eddies in the south (north) of 35°N.
2. From the eddy data set, we find that the eddies with lifetimes longer than 50 weeks have such features: more cyclonic (anticyclonic) eddies in the south (north) of 35°N in the KE (Figure 17). Again, from the relationship between the eddy size and eddy radius (Figure 15), eddy size is generally about 100 km when their lifetimes are longer than 50 weeks.
3. From the above two steps, it can be inferred that most eddies formed from the Kuroshio path meanders live much longer and have larger sizes than those eddies formed through other mechanisms.

According to the above discussion, one can see that eddies induced by the flow shear and the Kuroshio meander are different in terms of their sizes and lifetimes: Eddies induced by the flow shear are smaller and have short time than those by the Kuroshio meander. It should be noted that the eddies pinching off the Kuroshio can only happen in the meander Kuroshio. When the flow shear generates eddies, the Kuroshio cannot stay straight due to the loss of the pressure balance between the two sides of the Kuroshio and then the Kuroshio path meanders resulting in eddies pinching off the Kuroshio.

Figure 18 shows two cases how meanders of the Kuroshio path evolve into eddies (cyclonic and anticyclonic).

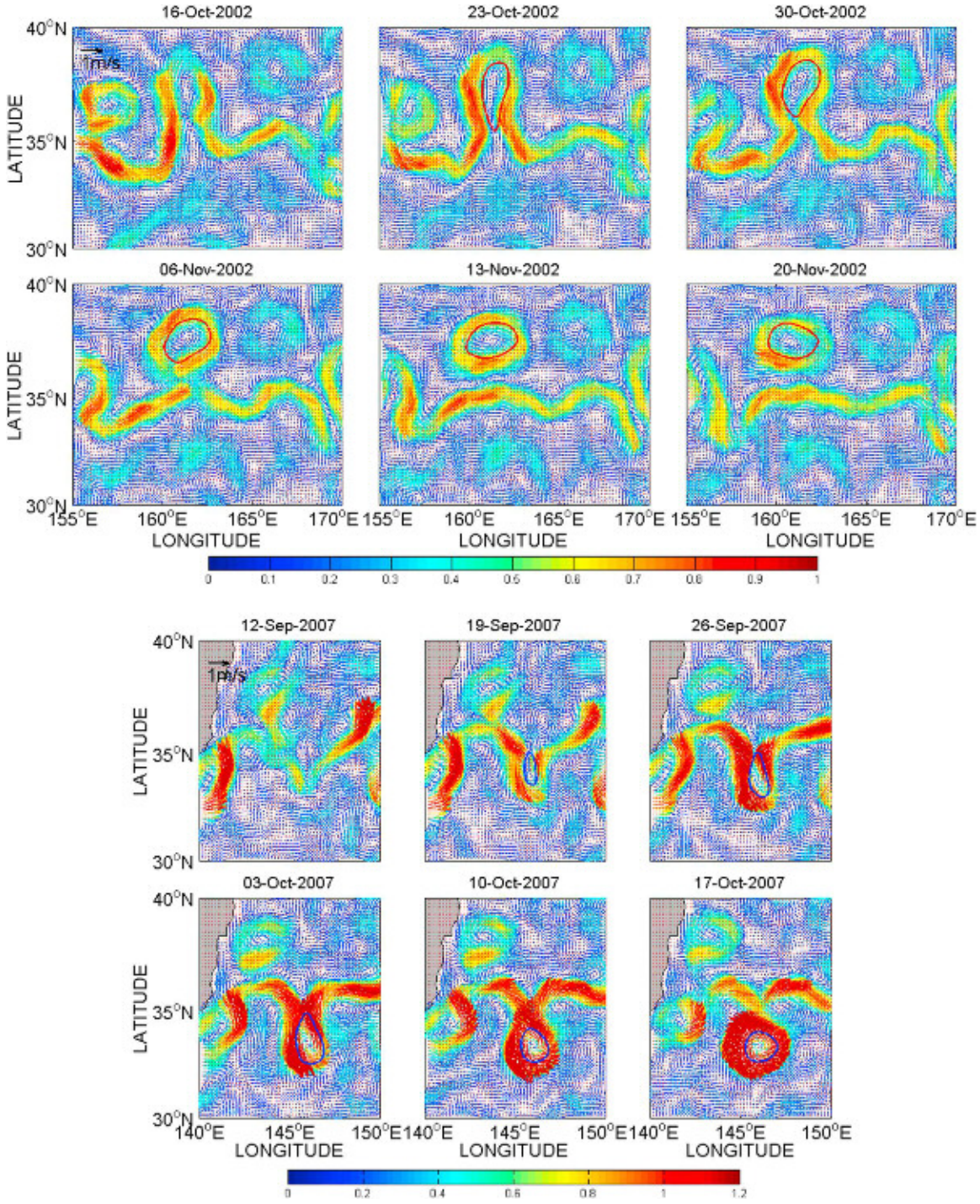

Figure 18. Eddy generated when a large Kuroshio meander pinches off. Vectors are surface geostrophic velocity anomalies. The figure sequence in the upper panel shows the creation of an anticyclonic eddy (red ring), and the sequence in the lower panel shows the creation of a cyclonic eddy (blue ring).

The instability caused by the horizontal velocity shear is also known as barotropic instability, in which the eddy (the disturbance) extracts energy from the mean flow. The meander of the Kuroshio can be considered as the nonlinear stage of flow instability, which could be caused by either baroclinic instability, or barotropic instability, or both. For the baroclinic instability, an eddy extracts energy from the available potential energy. The available potential energy is stored in the horizontal gradient of the

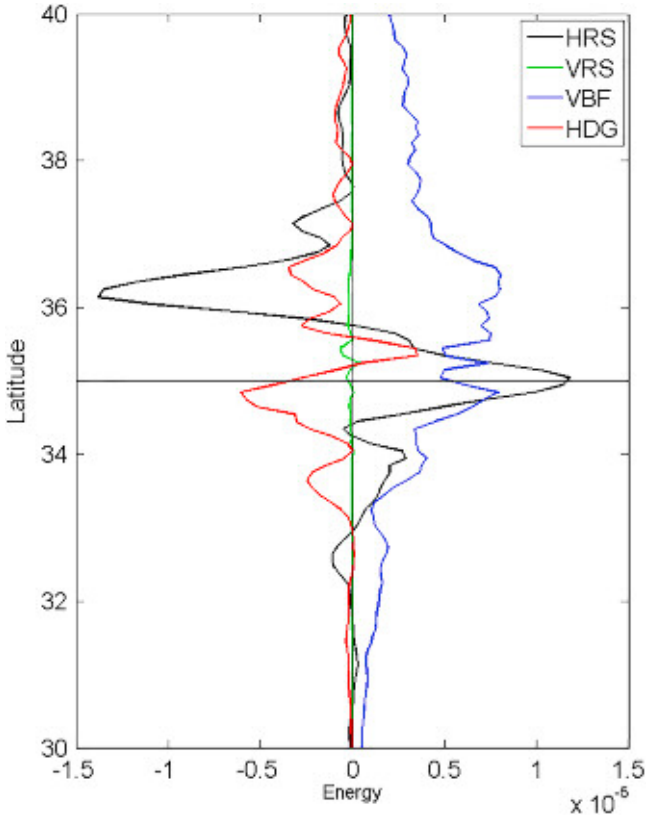

Figure 19. Variations of VBF (blue line), VRS (green line), HRS (black line) and HDG (red line) with the latitude. HDG = horizontal density gradient source; HRS = horizontal shear source; VBF = vertical buoyancy flux; VRS = vertical shear source.

density, which is accompanied by the vertical shear of the flow, according to the thermal wind relationship.

The long-lived large eddies are known as *rings* (Fuglister, 1963). They are caused by hydrodynamic instability, which occurs essentially when the Kuroshio Current keep its geostrophic balance (pressure gradients balanced by Coriolis accelerations) (Olson, 1991). Rings are preceded by growing waves or meanders. The Gulf Stream meander growth leads to cyclonic eddies (cold-core rings) separate from the Gulf Stream in the south and migrate southward, and northward of the stream to form anticyclonic (warm-core) eddies (e.g., Enikeev & Mikhailichenko Yu, 1990; Lee et al., 1991).

In order to better understand the eddy generation mechanism, we estimate the EKE sources through the EKE evolution equation, which is expressed as (Harrison & Robinson, 1978; Oey, 2008)

$$\frac{\mathrm{d}(EKE+EPE)}{\mathrm{d}t} = HRS + VRS + VBF + HGD + Diffusion, \tag{6}$$

$$\text{where horizontal shear source } HRS = -\overline{\mathbf{u}'v'}\cdot\frac{\partial\overline{\mathbf{u}}}{\partial y} - \overline{\mathbf{u}'u'}\cdot\frac{\partial\overline{\mathbf{u}}}{\partial x}, \tag{7}$$

$$\text{vertical shear source } VRS = -\overline{\mathbf{u}'w'}\cdot\frac{\partial\overline{\mathbf{u}}}{\partial z}, \tag{8}$$

$$\text{vertical buoyancy flux } VBF = \overline{w'b'}, \tag{9}$$

$$\text{and horizontal density gradient source } HDG = -\frac{g^2}{\rho_0^2 N^2}\left(\overline{u'\rho'}\frac{\partial\overline{\rho}}{\partial x} + \overline{v'\rho'}\frac{\partial\overline{\rho}}{\partial y}\right), \tag{10}$$

where u and v, w are the horizontal and vertical velocities, respectively; b is buoyancy; N is buoyancy frequency; and ρ_0 is the density of seawater. Prime denotes the anomaly with respect to the 1-year mean (seasonal signals are removed). The overbar denotes the 1-year mean.

Due to the limit of satellite data, we use the OFES data instead of AVISO to do the EKE evolution analysis. To verify that the OFES data are consistent with AVISO data, we apply the eddy detection scheme to OFES data and compare them with results from AVISO data. They show similar patterns as those from AVISO. Please see the details in Appendix A. From the analysis of 1-year OFES data, we can see that the surface Kuroshio Current runs along the 35° with oscillation. We use OFES upper layers velocity and density data (depth $<$ 200 m) to calculate the value of HRS, VRS, and VBF of each layer based on the equations (7)–(9). The vertical integral and zonal averages are then calculated to obtain the EKE sources varying with latitude; see Figure 19. From Figure 19, it is obviously that VRS is almost 0, the VBF value always is positive, and HRS is dominant within 1° away from 35°N. The positive values imply that the eddies withdraw energy from the mean flow. The dominant HRS shows that the shear instability occurs at the edges of the Kuroshio. The vertical buoyancy fluxes represent the occurrence of baroclinic instability. The results support our deduction on eddy generation mechanisms.

In summary, the two eddies-generating mechanisms (shear instability and meander instability) can be identified through different eddy characteristics. The baroclinic instability could also play a role in eddy generation, but it cannot be confirmed through eddy data analysis since it requires numerical modeling research. Flow shear generates small and short-lived eddies, cyclonic to the north and anticyclonic to the south of the Kuroshio mean path, while the Kuroshio meander generates larger and longer-lived eddies, which are anticyclonic to the north and cyclonic to the south.

5. Summary

In this study, we applied the eddy geometry-based automated detection scheme developed by Nencioli et al. (2010) to the altimetry-measured SSHA data in the extended KE region during the period of 1993–2012. We followed eddies throughout their lifetimes, from generation to dissipation and obtained a data set including 7,574 eddies with lifetimes longer than or equal to 4 weeks. Together with the Argo profiles, the study advances our understanding of the eddy activities in the KE region from previous studies such as Itoh and Yasuda (2010), Dong, Nencioli, et al. (2011), and Dong, Liu, et al. (2011): more detailed eddy statistical characteristics, eddy impacts on the stratification, and eddy generation mechanisms.

A statistical analysis showed that the longest-lived cyclonic eddy survived for 142 weeks and the longest-lived anticyclonic eddy for 160 weeks. This shows that some eddies in the KE region have a very coherent structure and can persist for more than 2 years. Some eddies had a distribution of sizes that was found to be well described by the lognormal distribution. Yet its significance remains to be understood. The peak radius for both cyclonic and anticyclonic eddies was found to be approximately 40 km. The peak values of the normalized relative vorticity of anticyclonic and cyclonic eddies were equal and opposite, and about 0.1 in magnitude (much less than one unit), implying that they are in approximate geostrophic balance. Agro floats were collocated with the eddies. The vertical profiles of the temperature and salinity of the collocated floats show that cyclonic (anticyclonic) eddies can cause negative (positive). The normalized eddy characteristics showed that all detected eddies passed through three stages from generation to dissipation, namely, youth, mature, and old. In the KE region, two potential eddy generation mechanisms were proposed: horizontal shear instability (barotropic instability) and instability in the path meanders, which is a nonlinear stage of an instability process. We found that cyclonic (anticyclonic) eddies with lifetime longer than 50 weeks exist at latitudes equatorward (poleward) of 35°N. However, when the eddy lifetimes are shorter than 20 weeks, the opposite result is observed: Cyclonic (anticyclonic) eddies exist at latitudes poleward (equatorward) of 35°N. We further apply an eddy-resolving numerical product to quantitatively analyze the eddy generation mechanisms.

Appendix A: Eddy Characteristic Analysis with OFES Data

We apply the eddy detection scheme to OFES data and compare them with results from AVISO data; see Figures A1–A3. They show similar patterns as those from AVISO.

Figure A4 is the latitudinal variation of the number of eddies with lifetimes shorter than 20 weeks: anticyclonic (left panel) and cyclonic (right panel) eddies. And Figure A5 is the eddy trajectories for eddies with lifetime longer than 50 weeks. Comparing the result with AVISO eddy database, they show similar patterns.

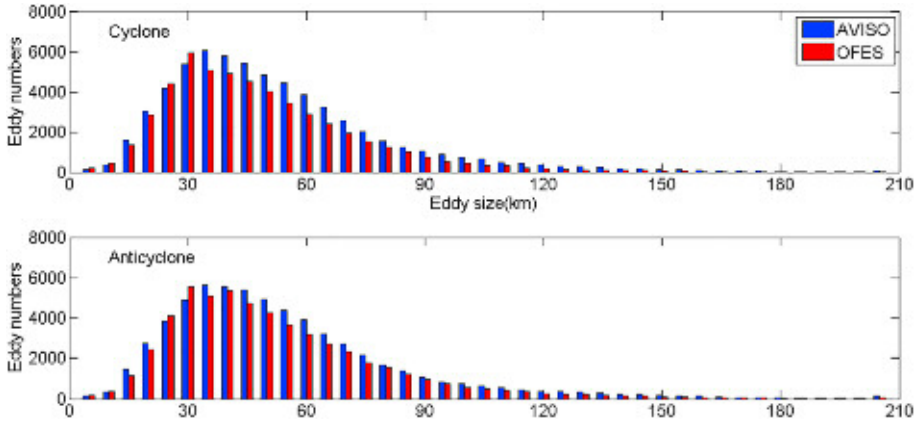

Figure A1. Histograms of eddy size. (top) cyclone. (bottom) anticyclone. AVISO = Archiving, Validation and Interpretation of Satellite Oceanographic; OFES = Ocean General Circulation Model for the Earth Simulation.

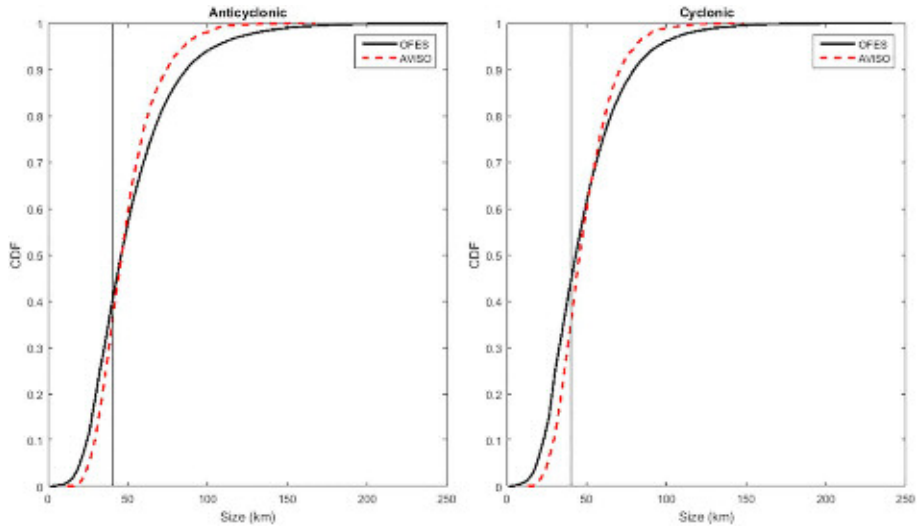

Figure A2. Cumulative probability distribution of eddy size for the comparison between the OFES and AVISO data. (left) Anticyclone. (right) Cyclone. AVISO = Archiving, Validation and Interpretation of Satellite Oceanographic; OFES = Ocean General Circulation Model for the Earth Simulation.

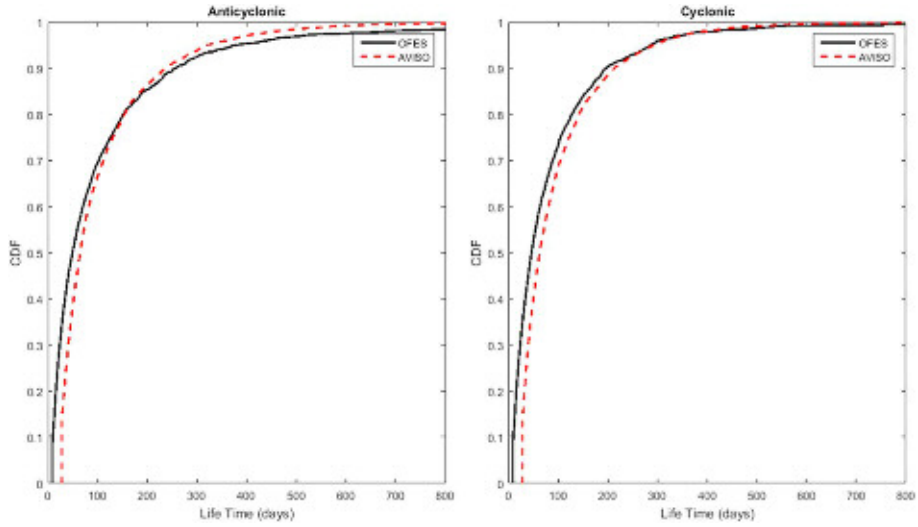

Figure A3. Cumulative probability distribution of eddy lifetime for the comparison between the OFES and AVISO data. (left) Anticyclone. (right) Cyclone. AVISO = Archiving, Validation and Interpretation of Satellite Oceanographic; OFES = Ocean General Circulation Model for the Earth Simulation.

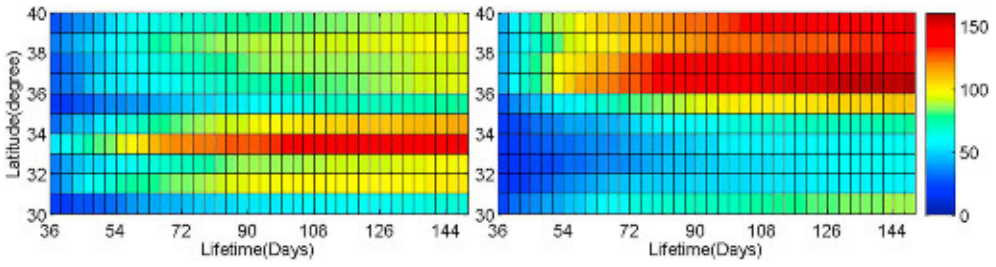

Figure A4. Latitudinal variation of the number of eddies with lifetimes shorter than 20 weeks: anticyclonic (left panel) and cyclonic (right panel) eddies.

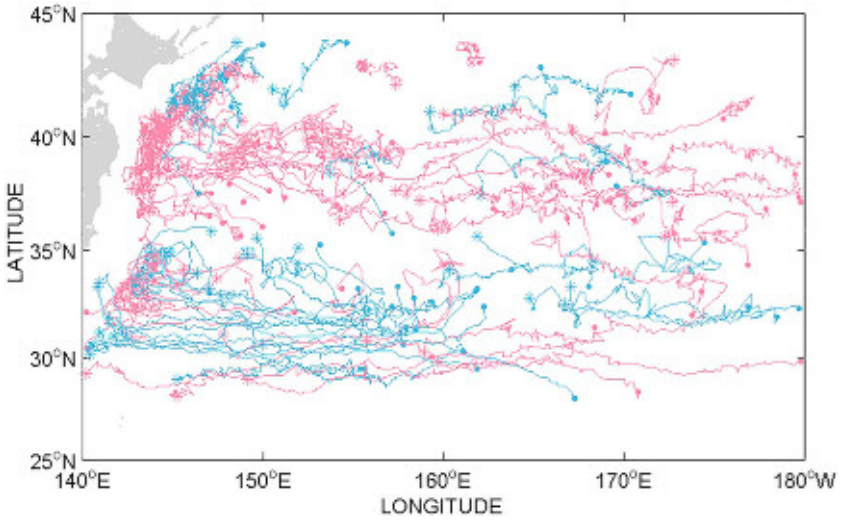

Figure A5. Eddy trajectories of eddies with lifetimes longer than 50 weeks. The dots and asterisks indicate the generation and termination points of each eddy trajectory, respectively. The red lines are anticyclonic eddies and blue lines are cyclonic eddies.

Acknowledgments
This research work was supported by National Key Research Program of China (2017YFA0604100, 2016YFC1401407, and 2016YFA0601803), NSFC (41476022, 41490643, 41621064 and 91528304), Jiangsu Province Science Foundation for Youths (BK20150897), Startup Foundation for Introducing Talent of Nanjing University of Information Science and Technology (2013r121, 2014r072), Program for Innovation Research and Entrepreneurship Teams in Jiangsu Province, the National Basic Research Program (2013CB430302), the National Natural Science Foundation of China (41321004, 91528304, and 41606022, the National ScienceFoundation of China for Outstanding Young Scientist under Grant 41622604,the Excellent Youth Science Foundation of Jiangsu Province under Grant BK2016090,), the National Program on Global Change and Air-Sea Interaction (GASI- IPOVAI-02, GASI- IPOVAI-04 and GASI- IPOVAI-05) National 973 Program of China (2014CB745000),Postgraduate Research & Practice Innovation Program of Jiangsu Province (KYLX16_0925), China Ocean Mineral Resources Research and Development Association program (DY135-E2-3-01), and the Natural Science Foundation of Jiangsu Province (BK20150897). We are grateful to AVISO (http://www.aviso.altimetry.fr/) for providing us with the SSHA data, Argo (http://doi.org/10.17882/42182) for providing us with the *T*/*S* profile data, and OFES (http://www.jamstec.go.jp/ofes/) for providing us with the 54 layers oceanic parameters data (*U*, *V*, *W*, *T*, and *S*). We would like to thank the anonymous reviewers for their constructive comments that greatly improved the manuscript.

Author Contributions

J. L. and C. D. initiated the idea, designed the study, analyzed the data, and contributed to the writing of the manuscript. B. Z. and D. C. aided in the development of the analysis techniques and contributed to the writing of the manuscript. Y. L., B. Z., G. K., and G. X. analyzed the data.

References

Amores, A., Monserrat, S., & Marcos, M. (2013). Vertical structure and temporal evolution of an anticyclonic eddy in the Balearic Sea (western Mediterranean). *Journal of Geophysical Research: Oceans*, *118*, 2097–2106. https://doi.org/10.1002/jgrc.20150

Bishop, S. P. (2013). Divergent eddy heat fluxes in the Kuroshio extension at 144-148E. Part II: Spatiotemporal variability. *Journal of Physical Oceanography*, *43*(11), 2416–2431. https://doi.org/10.1175/JPO-D-13-061.1

Bishop, S. P., Watts, D. R., & Donohue, K. A. (2013). Divergent eddy heat fluxes in the Kuroshio Extension at 144°–148°E. Part I: Mean structure. *Journal of Physical Oceanography*, *43*(8), 1533–1550. https://doi.org/10.1175/JPO-D-12-0221.1

Carton, X. (2001). Hydrodynamical modeling of oceanic vortices. *Surveys in Geophysics*, *22*(3), 179–263. https://doi.org/10.1023/A:1013779219578

Chelton, D. B., deSzoeke, R. A., Schlax, M. G., Karim, E. N., & Siwertz, N. (1998). Geographical variability of the first baroclinic Rossby radius of deformation. *Journal of Physical Oceanography*, *28*(3), 433–460. https://doi.org/10.1175/1520-0485(1998)028<0433:GVOTFB>2.0.CO;2

Chelton, D. B., Schlax, M. G., & Samelson, R. M. (2011). Global observations of nonlinear mesoscale eddies. *Progress in Oceanography*, *91*(2), 167–216. https://doi.org/10.1016/j.pocean.2011.01.002

Chelton, D. B., Schlax, M. G., Samelson, R. M., & deSzoeke, R. A. (2007). Global observations of large oceanic eddies. *Geophysical Research Letters*, *34*, L15606. https://doi.org/10.1029/2007GL030812

Chen, G., Li, Y., Xie, Q., & Wang, D. (2018). Origins of eddy kinetic energy in the Bay of Bengal. *Journal of Geophysical Research: Oceans*, *123*, 2097–2115. https://doi.org/10.1002/2017JC013455

Chen, G. X., Gan, J. P., Xie, Q., & Chu, X. Q. (2012). Eddy heat and salt transports in the South China Sea and their seasonal modulations. *Journal of Geophysical Research*, *117*, C05021. https://doi.org/10.1029/2011JC007724

Chen, G. X., Hou, Y. J., & Chu, X. Q. (2011). Mesoscale eddies in the South China Sea: Mean properties, spatio-temporal variability and impact on thermohaline structure. *Journal of Geophysical Research*, *116*, C06018. https://doi.org/10.1029/2010JC006716

Chen, G. X., Wang, D. X., & Hou, Y. J. (2012). The features and interannual variability mechanism of mesoscale eddies in the Bay of Bengal. *Continental Shelf Research*, *47*, 178–185. https://doi.org/10.1016/j.csr.2012.07.011

Chow, C. H., Tseng, Y. H., Hsu, H. H., & Young, C. C. (2017). Interannual variability of the subtropical countercurrent eddies in the north pacific associated with the western-pacific teleconnection pattern. *Continental Shelf Research*, *143*, 175–184. https://doi.org/10.1016/j.csr.2016.08.006

Chu, X., Dong, C., & Qi, Y. (2017). The influence of ENSO on an oceanic eddy pair in the South China Sea. *Journal of Geophysical Research: Oceans*, *122*, 1643–1652. https://doi.org/10.1002/2016JC01264

Chu, X. Q., Xue, H. J., Qi, Y. Q., Chen, G. X., Mao, Q. W., Wang, D. X., & Chai, F. (2014). An exceptional anticyclonic eddy in the South China Sea in 2010. *Journal of Geophysical Research: Oceans*, *119*, 881–897. https://doi.org/10.1002/2013JC009314

Couvelard, X., Caldeirab, R. M. A., Araújo, I. B., & Tomác, R. (2012). Wind mediated vorticity-generation and eddy-confinement, leeward of the Madeira Island: 2008 numerical case study. *Dynamics of Atmospheres and Oceans*, *58*, 128–149. https://doi.org/10.1016/j.dynatmoce.2012.09.005

Dong, C. M., Lin, X. Y., Liu, Y., Nencioli, F., Chao, Y., Guan, Y. P., et al. (2012). Three-dimensional eddy analysis in the Southern California Bight. *Journal of Geophysical Research*, *117*, C00H14. https://doi.org/10.1029/2011JC007354

Dong, C. M., Liu, Y., Lumpkin, R., Lankhorst, M., Chen, D. K., McWilliams, J. C., & Guan, Y. P. (2011). A scheme to identify loops from trajectories of oceanic surface drifters: An application in the Kuroshio Extension region. *Journal of Atmospheric and Oceanic Technology*, *28*(9), 1167–1176. https://doi.org/10.1175/JTECH-D-10-05028.1

Dong, C. M., Mavor, T., Nencioli, F., Jiang, S., Uchiyama, Y., McWilliams, J. C., et al. (2009). An oceanic cyclonic eddy on the lee side of Lanai Island, Hawai'i. *Journal of Geophysical Research*, *114*, C10008. https://doi.org/10.1029/2009JC005346

Dong, C. M., McWilliams, J. C., Liu, Y., & Chen, D. K. (2014). Global heat and salt transports by eddy movement. *Nature Communications*, *5*(1), 3294. https://doi.org/10.1038/ncomms4294

Dong, C. M., Nencioli, F., Liu, Y., & McWilliams, J. C. (2011). An automated approach to detect oceanic eddies from satellite remotely sensed sea surface temperature data. *IEEE Geoscience and Remote Sensing Letters*, *8*(6), 1055–1059. https://doi.org/10.1109/LGRS.2011.2155029

Dong, G., & Chan, T. L. (2007). Large eddy simulation of flow structures and pollutant dispersion in the near-wake region of a light-duty diesel vehicle. *Atmospheric Environment*, *40*(6), 1104–1116.

Drazin, P. G., & Reid, W. H. (1981). *Hydrodynamic stability*. Cambridge: Cambridge University Press.

Enikeev, V. K. H., & Mikhailichenko Yu, G. (1990). On anticyclonic spin-off eddies in the Gulf Stream. *Sov. Journal of Physical Oceanography*, *I*(4), 303–307.

Fuglister, F. C. (1963). Gulf Stream '60. *Progress in Oceanography*, *1*, 265–373. https://doi.org/10.1016/0079-6611(63)90007-7

Gaube, P., Mcgillicuddy, D. J., Chelton, D. B., Behrenfeld, M. J., & Strutton, P. G. (2015). Regional variations in the influence of mesoscale eddies on near-surface chlorophyll. *Journal of Geophysical Research: Oceans*, *119*, 8195–8220. https://doi.org/10.1002/2014JC010111

Graves, L. P., McWilliams, J. C., & Montgomery, M. T. (2006). Vortex evolution due to straining: A mechanism for dominance of strong, interior anticyclones. *Geophysical and Astrophysical Fluid Dynamics*, *100*(3), 151–183.

Gruber, N., Lachkar, Z., Frenzel, H., Marchesiello, P., Munnich, M., McWilliams, J. C., et al. (2011). Eddy-induced reduction of biological production in eastern boundary upwelling systems. *Nature Geoscience*, *4*(11), 787–792. https://doi.org/10.1038/ngeo1273

Harrison, D., & Robinson, A. R. (1978). Energy analysis of open regions of turbulent flows: Mean eddy energetics of a numerical ocean circulation experiment. *Dynamics of Atmospheres and Oceans*, *2*, 185–211.

Hurlburt, H. E., Wallcraft, A., Schmitz, W., Hogan, P., & Metzger, E. (1996). Dynamics of the Kuroshio/Oyashio current system using eddy-resolving models of the North Pacific Ocean. *Journal of Geophysical Research*, *101*, 941–976. https://doi.org/10.1029/95JC01674

Ichikawa, K., & Imawaki, S. (1994). Life history of a cyclonic ring detached from the Kuroshio Extension as seen by the Geosat altimeter. *Journal of Geophysical Research*, *99*, 15,953–15,966. https://doi.org/10.1029/94JC01139

Itoh, S., & Yasuda, I. (2010). Characteristics of mesoscale eddies in the Kuroshio-Oyashio Extension region detected from the distribution of the sea surface height anomaly. *Journal of Physical Oceanography*, *40*(5), 1018–1034. https://doi.org/10.1175/2009JPO4265.1

Johnson, G. C., & McTaggart, K. E. (2010). Equatorial Pacific 13°C water eddies in the eastern subtropical South Pacific Ocean. *Journal of Physical Oceanography*, *40*(1), 226–236. https://doi.org/10.1175/2009JPO4287.1

Kobashi, F., Onikata, Y., Iwasaka, N., Kawai, Y., Oka, E., Uehara, K., et al. (2016). Small meanders of the kuroshio extension and associated northward spreading of warm water: Three-vessel simultaneous observations and an eddy-resolving ocean model simulation. *Journal of Geophysical Research: Oceans*, *121*, 5315–5337. https://doi.org/10.1002/2016JC011969

Kouketsu, S., Kaneko, H., Okunishi, T., Sasaoka, K., Itoh, S., Inoue, R., & Ueno4, H. (2016). Mesoscale eddy effects on temporal variability of surface chlorophyll a, in the Kuroshio extension. *Journal of Physical Oceanography*, *72*(3), 439–451. https://doi.org/10.1007/s10872-015-0286-4

Lee, T. N., Yoder, J. A., & Atkinson, L. P. (1991). Gulf Stream frontal eddy influence on productivity of the southeast U.S. continental shelf. *Journal of Geophysical Research*, *96*, 22,191–22,205. https://doi.org/10.1029/91JC02450

Lin, X. Y., Dong, C. M., Chen, D. K., Liu, Y., Yang, J. S., Zou, B., & Guan, Y. P. (2015). Three-dimensional properties of mesoscale eddies in the South China Sea based on eddy-resolving model output. *Deep-Sea Research Part I: Oceanographic Research Papers*, *99*(46–64), 46–64. https://doi.org/10.1016/j.dsr.2015.01.007

Liu, Y., Dong, C., Liu, X., & Dong, J. (2017). Antisymmetry of oceanic eddies across the Kuroshio over a shelfbreak. *Scientific Reports*, *7*(1), 6761. https://doi.org/10.1038/s41598-017-07059-1

Liu, Y., Dong, C. M., Guan, Y. P., Chen, D. K., McWilliams, J. C., & Nencioli, F. (2012). Eddy analysis in the subtropical zonal band of the North Pacific Ocean. *Deep-Sea Research Part I: Oceanographic Research Papers*, *68*, 54–67. https://doi.org/10.1016/j.dsr.2012.06.001

Ma, J., Xu, H., Dong, C., Lin, P., & Liu, Y. (2015). Atmospheric responses to oceanic eddies in the Kuroshio Extension region. *Journal of Geophysical Research: Atmospheres*, *120*, 6313–6330. https://doi.org/10.1002/2014JD022930

Masumoto, Y., Sasaki, H., Kagimoto, T., Komori, N., Ishida, A., Sasai, Y., et al. (2004). A fifty-year eddy-resolving simulation of the world ocean—Preliminary outcomes of OFES (OGCM for the Earth Simulator). *J. Earth Simulator*, *1*, 35–56.

Mishra, P., Sainz-Trapaga, S., & Sugimoto, T. (1999). Evolution of Kuroshio warm-core ring 93A from hydrographical propagation. Ecosystem Dynamics (Pembroke, Ont.) Dynamics of the Kuroshio–Oyashio Transition The Region: Proceedings of the International Marine Science Symposium, M. Terazaki et al., Eds., Japan Marine Science Foundation, 74–85.

Mitsudera, H., Waseda, T., Yoshikawa, Y., & Taguchi, B. (2001). Anticyclonic eddies and Kuroshio meander formation. *Geophysical Research Letters*, *28*, 2025–2028. https://doi.org/10.1029/2000GL012668

Miyazawa, Y., Guo, X., & Yamagata, T. (2004). Roles of mesoscale eddies in the Kuroshio paths. *Journal of Physical Oceanography*, *34*(10), 2203–2222. https://doi.org/10.1175/1520-0485(2004)034<2203:ROMEIT>2.0.CO;2

Miyazawa, Y., Kagimoto, T., Guo, X., & Sakuma, H. (2008). The Kuroshio large meander formation in 2004 analyzed by an eddy–resolving ocean forecast system. *Journal of Geophysical Research*, *113*, C10015. https://doi.org/10.1029/2007JC004226

Mizuno, K., & White, W. B. (1983). Annual and interannual variability in the Kuroshio Current system. *Journal of Physical Oceanography*, *13*(10), 1847–1867. https://doi.org/10.1175/1520-0485(1983)013<1847:AAIVIT>2.0.CO;2

Nencioli, F., Dong, C. M., Dickey, T., Washburn, L., & McWilliams, J. C. (2010). A vector geometry based eddy detection algorithm and its application to high-resolution numerical model products and high-frequency radar surface velocities in the Southern California Bight. *Journal of Atmospheric and Oceanic Technology*, *27*(3), 564–579. https://doi.org/10.1175/2009JTECHO725.1

Oey, L. Y. (2008). Loop current and deep eddies. *Journal of Physical Oceanography*, *38*(7), 1426–1449. https://doi.org/10.1175/2007JPO3818.1

Okubo, A. (1970). Horizontal dispersion of floatable particles in the vicinity of velocity singularities such as convergences. *Deep Sea Research and Oceanographic Abstracts*, *17*(3), 445–454.

Olson, D. B. (1991). Rings in the ocean. *Annual Review of Earth and Planetary Sciences*, *19*(1), 283–311. https://doi.org/10.1146/annurev.ea.19.050191.001435

Pegliasco, C., Chaigneau, A., & MorrowMain, R. (2015). Main eddy vertical structures observed in the four major eastern boundary upwelling systems. *Journal of Geophysical Research: Oceans*, *120*, 6008–6033. https://doi.org/10.1002/2015JC010950

Peliz, A., Boutov, D., & Teles-Machado, A. (2013). The Alboran Sea mesoscale in a long term high resolution simulation: Statistical analysis. *Ocean Modelling*, *72*, 32–52. https://doi.org/10.1016/j.ocemod.2013.07.002

Perret, L., Delville, J., Manceau, R., & Bonnet, J. P. (2006). Generation of turbulent inflow conditions for large eddy simulation from stereoscopic PIV measurements. *International Journal of Heat and Fluid Flow*, *27*(4), 576–584.

Prants, S. V., Budyansky, M. V., & Uleysky, M. Y. (2014). Lagrangian study of surface transport in the Kuroshio Extension area based on simulation of propagation of Fukushima-derived radionuclides. *Nonlinear Processes in Geophysics*, *21*(1), 279–289. https://doi.org/10.5194/npg-21-279-2014

Qiu, B., & Chen, S. (2005). Variability of the Kuroshio extension jet, recirculation gyre, and mesoscale eddies on decadal time scales. *Journal of Physical Oceanography*, *35*(11), 2090–2103. https://doi.org/10.1175/JPO2807.1

Qiu, B., & Chen, S. M. (2010). Eddy-mean flow interaction in the decadally modulating Kuroshio Extension system. *Deep Sea Research, Part II*, *57*(13-14), 1098–1110. https://doi.org/10.1016/j.dsr2.2008.11.036

Qiu, B., & Chen, S. M. (2011). Effect of decadal Kuroshio Extension jet and eddy variability on the modification of North Pacific intermediate water. *Journal of Physical Oceanography*, *41*(3), 503–515. https://doi.org/10.1175/2010JPO4575.1

Qiu, B., Chen, S. M., Wu, L. X., & Kida, S. (2015). Wind- versus eddy-forced regional sea level trends and variability in the North Pacific Ocean. *Journal of Climate*, *28*(4), 1561–1577. https://doi.org/10.1175/JCLI-D-14-00479.1

Roemmich, D., & Gilson, J. (2001). Eddy transport of heat and thermocline waters in the North Pacific: A key to interannual/decadal climate variability? *Journal of Physical Oceanography*, *31*, I3.

Scharffenberg, M. G., & Stammer, D. (2010). Seasonal variations of the large-scale geostrophic flow field and eddy kinetic energy inferred from the TOPEX/Poseidon and Jason-1tandem mission data. *Journal of Geophysical Research*, *115*, C02008. https://doi.org/10.1029/2008JC005242

Stammer, D. (1997). On eddy characteristic, eddy transports, and mean flow properties. *Journal of Notes and Correspondence*, *28*, 727–739.

Stammer, D., Böning, C., & Dieterich, C. (2001). The role or variable wind forcing in generating eddy energy in the North Atlantic. *Progress in Oceanography*, *48*(2-3), 289–311. https://doi.org/10.1016/S0079-6611(01)00008-8

Vaillancourt, R. D., Marra, J., Seki, M. P., Parsonsc, M. L., & Bidigared, R. R. (2003). Impact of a cyclonic eddy on phytoplankton community structure and photosynthetic competency in the subtropical North Pacific Ocean. *Deep Sea Research Part I: Oceanographic Research Papers*, *50*(7), 829–847. https://doi.org/10.1016/S0967-0637(03)00059-1

Volkov, D. L., Lee, T., & Fu, L. L. (2008). Eddy-induced meridional heat transport in the ocean. *Geophysical Research Letters*, *35*, L20601. https://doi.org/10.1029/2008GL035490

Wang, X. D., Li, W., Qi, Y. Q., & Han, G. J. (2012). Heat, salt and volume transports by eddies in the vicinity of the Luzon Strait. *Deep Sea Research Part I: Oceanographic Research Papers*, *61*, 21–33. https://doi.org/10.1016/j.dsr.2011.11.006

Waseda, T., Mitsudera, H., Taguchi, B., & Yoshikawa, Y. (2003). On the eddy-Kuroshio interaction: Meander formation process. *Journal of Geophysical Research*, *108*(C7), 3220. https://doi.org/10.1029/2002JC001583

Waterman, S., Hogg, N. G., & Jayne, S. R. (2011). Eddy-mean flow interaction in the Kuroshio extension region. *Journal of Physical Oceanography*, *41*(6), 1182–1208. https://doi.org/10.1175/2010JPO4564.1

Weiss, J. (1991). The dynamics of enstrophy transfer in 2-dimensional hydrodynamics. *Physica D*, *48*(2–3), 273–294. https://doi.org/10.1016/0167-2789(91)90088-Q

Xu, L., Li, P., Xie, S. P., Liu, Q., Cong, L., & Gao, W. (2016). Observing mesoscale eddy effects on mode-water subduction and transport in the north pacific. *Nature Communications*, *7*, 10505. https://doi.org/10.1038/ncomms10505

Yang, G., Yu, W. D., Yuan, Y. L., Zhao, X., Wang, F., & Chen, G. X. (2015). Characteristics, vertical structures, and heat/salt transports of mesoscale eddies in the southeastern tropical Indian Ocean. *Journal of Geophysical Research: Oceans*, *120*, 6733–6750. https://doi.org/10.1002/2015JC011130

Yang, Y., San Liang, X., Qiu, B., & Chen, S. (2017). On the decadal variability of the eddy kinetic energy in the Kuroshio extension. *Journal of Physical Oceanography*, *47*(5), 1169–1187. https://doi.org/10.1175/JPO-D-16-0201.1

Yasuda, I., Okuda, K., & Hirai, M. (1992). Evolution of a Kuroshio warm-core ring variability of the hydrographic structure. *Deep Sea Research*, *39*(11), S131–S161. https://doi.org/10.1016/S0198-0149(11)80009-9

Zhang, Z. G., Wang, W., & Qiu, B. (2014). Oceanic mass transport by mesoscale eddies. *Science*, *345*(6194), 322–324. https://doi.org/10.1126/science.1252418

Zhang, Z. W., Zhong, Y. S., Tian, J. W., Yang, Q. X., & Zhao, B. (2014). Estimation of eddy heat transport in the global ocean from Argo data. *Acta Oceanologica Sinica*, *33*(10), 42–47.